Geosci. Model Dev. Discuss., 2, 581–638, 2009
www.geosci-model-dev-discuss.net/2/581/2009/

Geoscientific Model Development Discussions

Geoscientific Model Development Discussions is the access reviewed discussion forum of *Geoscientific Model Development*

Icosahedral Shallow Water Model (ICOSWM): results of shallow water test cases and sensitivity to model parameters

P. Rípodas[1], A. Gassmann[2], J. Förstner[1], D. Majewski[1], M. Giorgetta[2], P. Korn[2], L. Kornblueh[2], H. Wan[2], G. Zängl[1], L. Bonaventura[2,*], and T. Heinze[1,]**

[1]Deutscher Wetterdienst, Offenbach, Germany
[2]Max Planck Institute for Meteorology, Hamburg, Germany
[*]now at: Politecnico di Milano, Milan, Italy
[**]now at: Freelance Scientist

Received: 19 May 2009 – Accepted: 26 May 2009 – Published: 16 June 2009

Correspondence to: P. Rípodas (maria-pilar.ripodas@dwd.de)

Published by Copernicus Publications on behalf of the European Geosciences Union.

Abstract

The Icosahedral Shallow Water Model (ICOSWM) has been a first step in the development of the ICON (acronym for ICOsahedral Nonhydrostatic) models. ICON is a joint project of the Max Planck Institute for Meteorology in Hamburg (MPI-M) and Deutscher Wetterdienst (DWD) for the development of new unified general circulation models for climate modeling and numerical weather forecasting on global or regional domains. A short description of ICOSWM is given. Standard test cases are used to test the performance of ICOSWM. The National Center for Atmospheric Research (NCAR) Spectral Transform Shallow Water Model (STSWM) has been used as reference for test cases without an analytical solution. The sensitivity of the model results to different model parameters is studied. The kinetic energy spectra are calculated and compared to the STSWM spectra. A comparison to the shallow water version of the current operational model GME at DWD is presented. In the framework of the ICON project an hydrostatic dynamical core has been developed, and a local grid refinement option and a non-hydrostatic dynamical core are under development. The results presented in this paper use the ICOSWM version at the end of 2008 and are a benchmark for the new options implemented in the development of these models.

1 Introduction

ICON (acronym for ICOsahedral Nonhydrostatic) is a joint project of the Max Planck Institute for Meteorology (MPI-M) and Deutscher Wetterdienst (DWD), the national weather service of Germany, for the development of new general circulation models. The project aims at unified general circulation models for climate modeling and numerical weather forecasting on global or regional domains. The new model will be based on finite volume and finite difference discretizations of the fully elastic, nonhydrostatic Navier-Stokes equations on geodesic, icosahedral, locally refinable grids. Various research institutes in Germany and elsewhere are also contributing to the project, among

GMDD

2, 581–638, 2009

which University of Postdam, Free University of Berlin and Los Alamos National Laboratory.

Bonaventura (2004) discussed the reasons that have led to the start of this new project with the goal to develop new models. The project joins DWD and MPI-M resources to face problems like mass conservation and monotonicity of tracer concentrations, local mesh refinement and the use of massively parallel computers for high resolution modeling.

As a first step, a shallow water model has been developed: the Icosahedral Shallow Water Model (ICOSWM). A first version of ICOSWM has been described in Bonaventura (2003, 2004) and Bonaventura et al. (2005). In Sect. 2 the main features of the model are given and the differences between the current version and the previous version in Bonaventura (2003, 2004) and Bonaventura et al. (2005) are highlighted.

To test the results of ICOSWM, the standard shallow water test suite of Williamson et al. (1992) is considered. In particular, results for test cases 2 (global steady state nonlinear zonal geostrophic flow), 5 (zonal flow over an isolated mountain) and 6 (Rossby-Haurwitz wave) of the standard shallow water test suite are shown in Sect. 3. Convergence of model errors for different grid resolutions are considered. Model results for test cases 5 and 6, that have no analytical solution, are compared to high resolution runs of a variant of the National Center for Atmospheric Research (NCAR) Spectral Transform Shallow Water Model (STSWM; Jakob-Chien et al., 1995). The sensitivity of the model results to different model parameters is studied. In Sect. 4 a comparison of results of ICOSWM and GMESWM, the shallow water version of the GME model (the current operational model at Deutscher Wetterdienst) is presented. Kinetic energy spectra for test cases 5 and 6 are shown in Sect. 5 and compared to the STSWM spectra.

GMDD
2, 581–638, 2009

2 Description of ICOSWM

Only a short description of the model is given here. Bonaventura (2003, 2004); Bonaventura et al. (2005) and Bonaventura and Ringler (2005) provide a detailed description of the model equations, the discrete operators and the spatial and time discretizations of a previous version of the ICOSWM model. Differences of the current version of ICOSWM to the model described in these references will be highlighted.

2.1 The model grid

The discretization method employed is defined as a special case of Delaunay triangulation on the sphere, i.e. the icosahedral geodesic grid described e.g. in Baumgardner and Frederickson (1985). The main reasons for the choice of this type of grid is its quasi-uniform coverage of the sphere, which solves automatically the pole problem of regular latitude-longitude grids. Furthermore its hierarchical structure provides a very natural setting for local grid refinement on nested grid hierarchies. Finite element approaches based on such geodesic grids have been introduced in Cullen (1974), Giraldo (2000), Heinze and Hense (2002). Finite volume approaches were presented in Heikes and Randall (1995a), Ringler et al. (2000), Ringler and Randall (2002).

The icosahedral construction yields a Delaunay triangulation of the sphere to which a Voronoi tessellation is naturally associated (see e.g. Quiang et al. (2003) and the references therein for a complete description of Delaunay-Voronoi grid pairs on the sphere), which consists of convex spherical polygons (either pentagons or hexagons, see Fig. 1). The triangular Delaunay grid is chosen as the primal grid and the pentagon-hexagon Voronoi grid as is the dual grid for ICOSWM.

The mass and vorticity preservation properties in ICON are achieved by use of triangular Delaunay cells on the sphere as control volumes and of the dual Voronoi cells (pentagons or hexagons) as control volumes for vorticity. The orthogonality of the primal and dual grid edges allows to use simple approximations of the gradient and rotation operators, in the framework of a C-type staggering of the discrete variables. This

GMDD
2, 581–638, 2009

represents a major change with respect to the discretization employed e.g. in GME (operational global model of Deutscher Wetterdienst, Majewski et al., 2002), where an A grid approach was used and discrete variables were defined at the vertices of the Delaunay grid and the orthogonality of primal and dual grids was not exploited.

In order to develop an analog of the rectangular C-type staggering (see e.g. Arakawa and Lamb, 1981; Lin and Rood, 1997; Ringler and Randall, 2002; Sadourny, 1975) on the Delaunay grids, the mass points are defined as the circumcenters of the triangular grid cells, while the velocity points are defined for each cell edge as the intersection between the edges of the Voronoi and Delaunay cells. (see Fig. 1). By construction, each of these points is equidistant from the centers of the Voronoi cells at the ends of that edge. In Fig. 2 *i* is a mass point, *l* is a velocity point and *v* is a vorticity point.

In a C grid discretization approach, the discrete prognostic variables considered are the value of the height field at the mass points (*i*), interpreted as a cell averaged value, and the velocity components normal to the triangle edges at the edge midpoints (*l*). The tangential velocity components, which are needed for the computation of the Coriolis force term, must be reconstructed.

The projection of the regular icosahedron on the sphere yields the so-called base grid or grid level-1. A first refinement step for which edges are divided in 2 or more, generally in n equal arcs, and connected by great circle arcs "parallel" to the edges of a parent cell, then results in the so called root grid, or grid level 0. Hence each cell of the base grid is divided in n^2 new triangular cells, or 4 cells if the original triangle edges are divided in two equal sections. From here on the grid construction allows only repeated bisection of triangular cell edges, yielding a hierarchy of computational grids numbered as grid levels 1, 2 etc. The number of cells quadruples at each refinement step. Note that this numbering of grid levels is different from that used in Bonaventura (2003, 2004) and Bonaventura et al. (2005). Figure 1 shows the triangles in red and hexagons/pentagons in blue of the root grid, or level 0 grid, resulting from an initial dyadic refinement step. Table 1 shows the numbers of mass points, velocity points and vorticity points of the different grid levels, again for a dyadic refinement of the base grid.

Since the velocity points are not equidistant from the adjacent Delaunay triangular grid cell centers, the difference operators described in Bonaventura et al. (2005) are only first order accurate. However, grid optimization procedures can partly cure this problem by reducing the off-centering to rather small values. The grid generator for the ICOSWM model has several optimization options (Gassmann and Heinze, 2007). In this paper only results for a grid optimized with the method suggested by Heikes and Randall (1995b) are shown.

In Table 2 the minimum, mean and maximum distances between mass points and between vorticity points for grid levels 0 to 6 for an Earth radius of 6.371229×10^6 m are shown for the case of a Heikes-Randall optimization of the icosahedral grid. The off-centering (%) of a velocity point is defined as

$$\text{off-centering} = 100 * \left| \frac{\text{d\_vel-mass}}{\text{d\_2massp}} - 0.5 \right| \quad (1)$$

where d_vel-mass is the distance between the velocity point and one of the adjacent mass points and d_2massp is the distance between the two adjacent mass points. In Table 2 the maximum of the velocity point off-centerings for each grid level is also given. The off-centering is reduced to rather small values for the higher grid levels. In Bonaventura (2003), Bonaventura (2004) and Bonaventura and Ringler (2005), the off-centering is defined as twice the value in Eq. (1).

2.2 Reconstruction of a vector field from the normal components

In order to recover the full velocity vector from the normal velocity components prescribed at the velocity points in a C grid variable staggering, a reconstruction procedure is needed. This is essential for the discretization of the shallow water equations, especially for the representation of the Coriolis force terms. We will always be concerned here with a vector field that is reconstructed at the triangular cell centers and whose normal components are assumed to be known at the edges of the triangles.

Two options are available in the ICOSWM model for the reconstruction, the Raviart-Thomas element of order 0 (RT0) and a Radial Basis Function reconstruction (RBF). In Bonaventura (2003, 2004) and Bonaventura et al. (2005), only the Raviart-Thomas reconstruction was available and used.

The Raviart-Thomas technique was introduced in Raviart and Thomas (1977) and a complete description of the mathematical properties can be found in Quarteroni and Valli (1994). The RBF reconstruction is described in Narcowich and Ward (1994) and Ruppert (2007). In this technique, a vector value function is interpolated with an interpolation function that is a linear combination of some functionals acting on a matrix valued Radial Basis Function. The matrix valued Radial Basic Function

$$\boldsymbol{\Phi} : \mathbb{R}^d \times \mathbb{R}^d \longrightarrow \mathbb{R}^{n\times n} \text{ is} \qquad (2)$$
$$\boldsymbol{\Phi}(\boldsymbol{x},\boldsymbol{y}) = (\Phi_{jk}(\|\boldsymbol{x}-\boldsymbol{y}\|))_{j,k=1\ldots n} \in \mathbb{R}^{n\times n}, \boldsymbol{x},\boldsymbol{y} \in \mathbb{R}^d$$

The RBF method is independent of the underlying data structure and can be applied to any spatially distrubuted data set.

In our implementation d=3, $\|\boldsymbol{x}-\boldsymbol{y}\|$ is the Euclidean distance and n is the number of points at which the normal component of the wind is used to reconstruct the wind vector at the cell triangular center. Several options are implemented for the kernel Φ (Gaussian, quadratic and inverse multiquadratic) and the number of points used for the reconstruction(3, 9 and 15 points stencil). Also a scale factor ε that defines a kind of influence radius of the RBF can be chosen (Φ_ε=$\Phi(r/\varepsilon)$), see Ruppert (2007). The influence of these parameters on the performance of ICOSWM is tested and shown in Sect. 3 .

2.3 Three-time-level semi-implicit time discretization

A three-time-level semi-implicit time discretization of the shallow water equations based on the leapfrog scheme is implemented in the model. The vector invariant form of the shallow water equations on the sphere has been chosen.

GMDD
2, 581–638, 2009

The geopotential gradients, the Coriolis force terms and the divergence of the velocity field are discretized implicitly, while an explicit time discretization is used for the nonlinear advection terms.

Asselin time filtering (see e.g. Asselin, 1972) has to be applied to filter computational modes of the leapfrog discretization, so that quantities at time level n are filtered as follows:

$$X_f^n = X^n + \epsilon(X_f^{n-1} - 2X^n + X^{n+1}), \tag{3}$$

where ϵ is a coefficient independent of the time step and of the resolution. Results of ICOSWM are shown in Sect. 3 for different values of ϵ (0.2–0.05).

In this paper all the results shown are for the three-time level semi-implicit scheme, while in Bonaventura (2003, 2004) and Bonaventura et al. (2005) a two-time-level semi-implicit time discretization is used. The three-time-level scheme is computationally more efficient and makes ICOSWM more comparable to the NCAR STSWM and GMESWM, that also employ a three-time-level scheme.

Discrete conservation properties have long been identified as an important feature of global circulation models (see e.g. Arakawa and Lamb, 1981; Lin and Rood, 1997; Ringler and Randall, 2002; Sadourny, 1975). The resulting numerical method conserves mass by construction. In Bonaventura and Ringler (2005) it is proved that the numerical method can be potential enstrophy conserving or total energy conserving. The tested model uses a simpler formulation which is essentially equivalent to the enstrophy preserving scheme of Bonaventura and Ringler (2005, Sect. 6 and 8) and produces indistinguishable results.

2.4 Numerical diffusion

An explicit diffusion term can be added to the right hand side of the prognostic variable equations. A linear fourth-order diffusion is applied to the velocity field. The time in which the shortest waves (highest wavenumber) resolved by the grid are reduced to a fraction of e^{-1} by the numerical diffusion is called e-folding time (τ). The analytical

relation between e-folding time and diffusion coefficient (k_4) for a quadrilateral grid is given by

$$k_4 = \frac{\Delta X^4}{(64 * \tau)} \tag{4}$$

where ΔX corresponds to the grid mesh.

Using a local value of the grid mesh, Eq. (4) gives a local value of the diffusion coefficient for a given e-folding time.

In the ICOSWM grid, the dual grid length or distance between mass points (dgl) and the primal grid length or distance between vorticity points (pgl) varies from point to point. In the model, Eq. (5) has been used to calculate a local diffusion coefficient at each velocity point.

$$k_4 = \frac{(dgl)^2 (\frac{pgl}{\sqrt{3}})^2}{(64 * \tau)} \tag{5}$$

Thus for a given grid level, a range of values for the diffusion coefficient is used, depending on the local grid mesh.

For a grid of equilateral triangles, the relation $dgl = (\frac{pgl}{\sqrt{3}})$ holds. Using it, the calculation of the local diffusion coefficients can be approximated by

$$k_4 \approx \frac{(dgl)^4}{(64 * \tau)} \tag{6}$$

Equation (6) can be used to estimate the minimum, mean and maximum values of the diffusion coefficients used in the model for different grid levels and e-folding times. These values are listed in Tables 3 and 4 for e-folding times of 28 and 2 h. The inhomogeneities of the grid edge lengths, which increase with resolution, translate to ratios between maximum to minimum diffusion coefficients of ~20 to ~30 for grid levels 2 to 6 , respectively.

GMDD
2, 581–638, 2009

3 Results of shallow water test cases

The standard shallow water test suite of Williamson et al. (1992) is a very useful benchmark for the model development process. This test suite comprises a number of idealized tests which are representative of some main features of large scale atmospheric motion. This section presents results for the steady state zonal geostrophic flow (test case 2), the zonal flow over an isolated mountain (test case 5) and the Rossby-Haurwitz Wave (test case 6).

The time steps are set to 1440, 720, 360, 180 and 90 s for grid levels 2, 3, 4, 5 and 6, respectively to yield similar Courant numbers at different grid levels. All the results presented here are obtained with the semi-implicit three-time level scheme and Heikes Randall optimized grid.

The normalized errors l_2, and l_∞ in Williamson et al. (1992) are used to test the model quantitatively. For the case of the height field, the expressions for the l_2, and l_∞ errors are

$$l_2(h) = \{I[(h(\lambda,\theta) - h_T(\lambda,\theta))^2]\}^{\frac{1}{2}} / \{I[(h_T(\lambda,\theta))^2]\}^{\frac{1}{2}} \quad (7)$$

$$l_\infty(h) = \max|h(\lambda,\theta) - h_T(\lambda,\theta)| / \max|h_T(\lambda,\theta)| \quad (8)$$

where λ and θ are the longitude and latitude of the grid points, h is the model output, h_T is the true solution if there is an analytical solution and a reference solution if not, and I is a discrete approximation to the global integral

$$I(h) = \int_0^{2\pi} \int_{-\frac{\pi}{2}}^{\frac{\pi}{2}} h(\lambda,\theta) \cos\theta d\theta d\lambda. \quad (9)$$

3.1 Williamson's test case 2 with zonal flow

Test case 2 of the standard shallow water suite of Williamson et al. (1992) is a steady state solution of the non-linear shallow water equations. It consists of a solid body

rotation or zonal flow with the corresponding geostrophic height field. The spherical coordinate poles are not necessarily coincident with earth rotation axis. We denote α the angle between the coordinate and rotational axis. For α=0 the flow is zonal and for $\alpha=\frac{\pi}{2}$ there is a flow over the pole. We consider here the case with zonal flow.

For this test case, an analytical solution is available, so that approximate convergence rates can be computed by applying the numerical method at different resolutions.

In the following convergence results for different sets of model parameters after 10 days simulation are presented.

3.1.1 Sensitivity to the e-folding time

We start to test the influence of using different e-folding times for the diffusion.

Several experiments have been run with different e-folding times (28, 12, 2 and 1 h) and also without diffusion ($\tau=\infty$).

The tests have been performed with Asselin filter parameter 0.1, RBF reconstruction with Gaussian kernel, 9 points stencil and scale factor 0.5.

A comparison of the convergence of the normalized errors for the height, and vorticity fields after 10 days runs for the different experiments is shown in Fig. 3. The results for the different e-folding times are plotted in different colours and in the order shown in the figure. As in the other convergence figures shown in this work, the black line represents a second order convergence and the l_2 and l_∞ normalized errors are represented with solid and dash-dotted lines respectively. The behavior of the l_1 errors is similar to the l_2 errors and it is not plotted for clearness.

The convergence plot for the wind field is not shown because no significant sensitivity to the e-folding time is observed in the normalized errors for this field. A second order convergence is observed for both l_2 and l_∞ (see Table 5).

In Fig. 3 (bottom) we observe that the normalized errors for the height field increase with decreasing e-folding times (increasing diffusion). The effect is larger in the case of the l_∞ error. A second order convergence is observed for both l_2 and l_∞.

In Fig. 3 (top) we observe the opposite effect in the case of the vorticity field. The errors are reduced with increasing diffusion coefficients (decreasing e-folding times), especially for the higher grid levels. In a geostrophic balance, the vorticity is proportional to the Laplacian of the height field, and therefore any small scale noise present in the height field is amplified in the vorticity field. Increasing diffusion reduces this noise, reducing at the same time the normalized errors for the vorticity field. For the vorticity field second order convergence is only achieved for the higher grid levels when high diffusion coefficients are used (e-folding times of the order of 2 h). The positive effect of a larger diffusion in the vorticity errors is larger than the negative effect in the height errors. Therefore a 2 h e-folding time seems to be a good choice. Smaller e-folding times are not recommended because the experiment with τ=1 h have larger errors for all the variables than the experiment with 2 h e-folding time. In the case of τ=1 h, the diffusion is smoothing too much.

Table 5 presents the numerical values of the normalized l_2 and l_∞ errors after 10 days for the different variables from grid level 2 to 6 for the experiment with 2 h e-folding time.

Figure 4 shows the error fields for height (bottom) and vorticity (top) for τ=∞, i.e. no explicit diffusion, RBF reconstruction with 9 points stencil and scale factor 0.5, Asselin parameter 0.1 and grid level 6. The height errors show a clear wavenumber-5 pattern due to the icosahedral grid. The vorticity errors also show a wavenumber-5 pattern with larger errors near the 12 original points of the icosahedron. These larger errors in the vorticity field near these points are reduced when explicit diffusion is applied, decreasing the l_2 and l_∞ normalized vorticity errors.

3.1.2 Sensitivity to the wind reconstruction

Some experiments have been run to test the sensitivity of ICOSWM to the way the wind field is reconstructed from the normal components of the wind to the center of the triangular cells.

For the RBF reconstruction, some parameters can be chosen. The radial basic functions used (the kernel), the stencil and a scale factor. For a detailed description of

these parameters see Ruppert (2007).

Experiments with the following wind reconstructions have been run:

- RBF Gaussian kernel, 3 points stencil, scale factor 1.
- RBF Gaussian kernel, 9 points stencil, scale factor 2.
- RBF Gaussian kernel, 9 points stencil, scale factor 5.
- RBF Gaussian kernel, 9 points stencil, scale factor 1.
- RBF Gaussian kernel, 15 points stencil, scale factor 5.
- Raviart-Thomas reconstruction (3 points stencil).
- RBF inverse multiquadratic kernel, 9 points stencil, scale factor 5.
- RBF inverse multiquadratic kernel, 9 points stencil, scale factor 2.

In all the experiments the e-folding time is 2 h and the Asselin filter is set to 0.1.

Figure 5 shows the convergence results for wind (bottom) and vorticity (top). The convergence for l_2 and l_∞ is shown with solid and dash-dotted lines respectively. As in the other convergence plots, each experiment is identified with a colour and the experiment results are plotted in the order shown in the figure.

The fact that most of the experiments give similar results means that a variety of RBF options can be chosen without changing the ICOSWM performance and is very positive. The experiments that lead to larger errors help to determine the range of values of the RBF options that are optimal for the reconstruction. The experiment with RBF reconstruction with a Gaussian kernel, 9 points stencil and scale factor 0.2 gave for all variables significantly larger l_2 and l_∞ errors. The RBF parameters in this experiment are considered not adequate because of the larger errors. The experiment with the inverse multiquadratic kernel, 9 points stencil and scale factor 0.2 also results in larger wind and vorticity l_2 errors and considerably larger vorticity l_∞ errors. This result can

GMDD
2, 581–638, 2009

be explained considering that the scale factor define a kind of influence radius of the RBF. A small scale factor means that the point where the wind is reconstructed can be far from the influence radius of some/all of the stencil points, resulting in large errors.

It is remarkable that the experiments with bigger stencils for the reconstruction (RBF 15 and 9 points stencil) do not have better results than the experiments with RBF 3 points stencil and Raviart-Thomas reconstruction. In fact the experiment with a 3 points stencil RBF reconstruction yields slightly better results. In this test case, the wind field is smooth, so a bigger stencil for the reconstruction does not improve the results.

We can conclude that in the case of the RBF reconstruction, the results do not depend significantly on the kernel and the stencil chosen. There is a range of scale factors that give similar good results. For the Gaussian kernel and 9 points stencil values from 0.5 to 1 seem to be adequate, and 0.5 is a good selection for the inverse multiquadratic kernel with 9 points stencil.

3.1.3 Sensitivity to the Asselin filter

Some experiments have been run for different Asselin filter parameters . All of these experiments use the semi-implicit three-time-level scheme, e-folding time of 2 h and RBF reconstruction with Gaussian kernel, 9 points stencil and scale factor 0.5. Asselin filter parameters 0.2, 0.1, 0.08, 0.05 and 0.03 have been considered.

The model simulations become numerically unstable for Asselin parameter 0.05 and 0.03 at grid levels 5 and 6. This means that we need an Asselin filter parameter bigger than 0.05.

The normalized errors l_2 and l_∞ for the height, wind and vorticity fields after 10 days are not exactly the same for all the experiments, but the differences are too small to be seen in a convergence plot. Thus a comparison of the convergence on accuracy for the different experiments is not shown.

We can conclude that there is no important effect of the Asselin filter, but it must be larger than 0.05 for numerical stability.

3.2 Williamson's test case 5

In test case 5 of Williamson et al. (1992) the initial state consists of a zonal flow impinging on an isolated mountain of conical shape. The surface or mountain height h_s is given by

$$h_s = h_{s_0}(1 - r/R) \tag{10}$$

where h_{s_0}=2000 m, $R=\pi/9$ and $r^2=\min[R^2,\ (\lambda-\lambda_c)^2+(\theta-\theta_c)^2]$. The center of the mountain is located at $\lambda_c=3\pi/2$ radians, $\theta_c=\pi/6$ radians.

The imbalance in the initial state and the presence of the mountain lead to the development of a Rossby gravity wave which propagates all around the globe. This test is relevant to understand the response of the numerical solution to orographic forcing and it has been a common benchmark since the development of the first spectral models (see e.g. Gill, 1982).

No analytical solution is available for this test case and a reference model is used to evaluate the errors of ICOSWM. As reference the NCAR STSWM has been used. The spectral resolution for the reference model is T426, the time step is 90 seconds, the diffusion coefficient is 4.97×10^{11} m^4 s^{-1} and no Asselin filter is applied. The reference solution is available at http://icon.enes.org/swm/stswm/node5.html.

For a variety of model parameters 15 days runs have been done. The spectral reference solution is interpolated by bi-cubic interpolation from the corresponding Gaussian grid (that has a resolution of 31.25 km at the Equator) to the ICOSWM grids at different grid levels. The difference between the ICOSWM output fields and the interpolated reference solution is used to calculate the l_2 and l_∞ normalized errors.

3.2.1 Sensitivity to the e-folding time

Experiments with different e-folding times (28 h and 2 h) and without explicit diffusion have been run. All of then use Asselin filter 0.1 and RBF reconstruction with Gaussian kernel, 9 points stencil and scale factor 0.5.

Figure 6 shows the height (bottom) and vorticity (top) fields after 15 days for the case of an e-folding time of 2 h and grid level 6. In the plot the mountain height is represented by black contour lines at intervals of 400 m.

Except for grid level 2, no significant influence of the e-folding time is observed in the height and wind errors in the three experiments. In the case of the vorticity field the l_2 errors are slightly smaller with larger diffusion coefficients for all the grid levels (see Fig. 7).

Table 6 shows the numerical values of the normalized errors after 15 days for the different variables from grid level 2 to 6 for the experiment with 2 h e-folding time.

A second order convergence for the height field is only achieved for the coarser resolutions. The l_2 errors for the wind and vorticity fields show a convergence rate slightly larger than first order. The l_∞ errors lose convergence for the higher resolutions.

Figure 8 shows the difference with respect to the reference STSWM solution for the vorticity field for grid level 6 (bottom) and grid level 5 (top) with e-folding time 2 h, RBF reconstruction with Gaussian kernel, 9 points stencil, scale factor 0.5 and Asselin parameter 0.1. The same colour table is used in both cases. The difference map does not show a wave number-5 pattern, as in test case 2. It seems to be related to the generation and/or propagation of the Rossby gravity waves generated by the presence of the mountain (center at 90° W, 30° N). The large differences at the north-east border of the mountain are differences in the intensity and location of the maximum of the vorticity between the outputs of ICOSWM and NCAR STSWM. The number of grid points with large errors is considerably reduced moving from grid level 5 to grid level 6, reducing the l_2 normalized error. But the largest error is only slightly reduced, and the convergence rate of the l_∞ error is very small.

3.2.2 Sensitivity to the wind reconstruction

As in test case 2, some experiments with different wind reconstructions have been run to evaluate the impact of the reconstruction technique in the model results. For simplicity, and considering the previous results for test case 2, only experiments with

Raviart-Thomas reconstruction and RBF with Gaussian kernel and different stencils and scale factors have been performed.

Figure 9 shows the l_2 (solid lines) and l_∞ (dash-dotted lines) normalized errors after 15 days for the height (bottom) and wind (top) fields for different grid levels. The l_2 and l_∞ errors with Raviart-Thomas and RBF 3 points stencil reconstruction are very similar, the convergence line for both experiments would be indistinguishable and the Raviart-Thomas experiment results are not represented in Fig. 9.

The two experiments with RBF 9 points stencil reconstruction and different scale factors also have very similar results. The 15 points stencil generally produces larger errors than a 9 points stencil. The difference in the errors is reduced with increasing grid level and at grid level 6 all the experiments have similar errors. In the case of the height field (and the vorticity field, not shown here), the errors using 15 or 3 points stencil are very similar. In the case of the wind field, the 15 points stencil reduces the wind errors for the higher grid levels compared to the 3 points stencil experiments.

From these results we can conclude that a 15 points stencil for the reconstruction does not improve significantly the results and is not recommended, as it is computationally more expensive.

3.2.3 Sensitivity to the Asselin filter

Experiments with different Asselin filter parameters (0.2, 0.1, 0.08 and 0.05) have been run, with semi-implicit three-time-level scheme, RBF reconstruction with Gaussian kernel, 9 points stencil, scale factor 0.5 and e-folding time of 2 h.

The convergence plots for l_2 (solid lines) and l_∞ (dash-dotted lines) after 15 days for the height and wind fields are shown in Fig. 10 bottom and top, respectively.

The normalized errors for the higher resolutions are significantly reduced with decreasing Asselin filter parameter, especially for the height l_2 and l_∞ normalized errors and the wind l_2 normalized errors. In the reference model the Asselin filter parameter is set to zero and the ICOSWM solution is closer to the reference model when a small Asselin filter parameter is used.

The experiment with Asselin parameter 0.05 can not be run for grid level 2. Smith and Dritschel (2006) report that they found a limit for the minimum value of the Asselin filter parameter that could be used in their model. This value is related to the mean short-scale gravity wave speed and depends on the time step. This minimum Asselin parameter increases with increasing time step. For grid level 2, the time step is 1440 s and 0.05 is slightly below the minimum Asselin parameter reported by Smith and Dritschel (2006).

No sensitivity to the Asselin filter parameter is observed in the case of the vorticity field normalized errors.

Following these results, 0.05 would be the best choice for the Asselin filter parameter.

3.3 Williamson's test case 6

In test case 6 of Williamson et al. (1992) the initial state consists of a Rossby-Haurwitz wave of wavenumber-4. This type of wave is an analytic solution for the barotropic vorticity equation and has also been widely used to test shallow water models, since the analysis in Hoskins (1973) supported the view that wavenumber-4 is stable also as a solution of the shallow water equations. However, some recent work presented in Thuburn and Li (2000) has shown that the Rossby-Haurwitz wave of test case 6 is actually unstable as a solution of the shallow water equations, since small random perturbations in the initial state result in long term disruption of the wavenumber-4 pattern. This was shown to be the case for a wide range of numerical models, including spectral transform models. Therefore, the usefulness of the Rossby-Haurwitz wave of wavenumber-4 as a benchmark for the solution of the shallow water initial value problem is limited to time ranges shorter than those sometimes considered in the literature. We choose a run time of 10 days.

Again the NCAR STSWM is used as a reference to evaluate the normalized errors of the ICOSWM. The spectral model resolution is T511, the time step is 90 seconds, the diffusion coefficient is $3.4\times10^{12}\,\mathrm{m}^4\,\mathrm{s}^{-1}$ and no Asselin filter is applied. The reference solution is available at http://icon.enes.org/swm/stswm/node5.html. The corresponding

Gaussian grid has a resolution of 26 km at the Equator. The explicit diffusion coefficient used in test case 6 to produce the STSWM reference solution is larger than in test case 5 to reduce the small scale noise in the vorticity field.

Convergence test after 10 days for runs with a variety of model parameters are shown.

3.3.1 Sensitivity to the e-folding time

Experiments with different e-folding times (28 h and 2 h) and without explicit diffusion have been run. All of then use Asselin filter 0.1 and RBF reconstruction with Gaussian kernel, 9 points stencil and scale factor 0.5.

Figure 11 shows the height field after 10 days for the case of an e-folding time of 2 h and grid level 6. The wavenumber 4 pattern is well kept after 10 days.

No important variability is observed for the l_2 and l_∞ errors of the wind field. In the case of the vorticity, the l_2 and l_∞ errors are reduced with larger diffusion coefficients (smaller e-folding times), see Fig. 12. In the case of the height field, the l_2 and l_∞ errors increase slightly with increasing diffusion but it can barely be seen in a convergence comparison plot.

Table 7 summarizes the numerical values of the normalized errors after 10 days for the different variables from grid level 2 to 6 for the experiment with 2 h e-folding time.

The l_2 and l_∞ normalized height errors show approximately second order convergence. This is also the case for the l_2 wind errors, but the l_∞ wind errors lose convergence for the higher grid levels. For the vorticity field, both the l_2 and l_∞ errors lose convergence for the higher grid levels.

Figure 13 shows the differences of ICOSWM with respect to the STSWM reference for the vorticity field after 10 days and grid level 6, with e-folding time 2 h, RBF reconstruction with 9 points stencil, scale factor 0.5 and Asselin parameter 0.1. The differences map shows a wavenumber-4 pattern and it is not related to the grid.

An e-folding time of 2 h is a good choice because of the smaller vorticity errors. The mean diffusion coefficient used for grid level 6 and e-folding time 2 h is

$3.18\times10^{12}\,m^4\,s^{-1}$ (see Table 4), very similar to the value used in the spectral reference model ($3.4\times10^{12}\,m^4\,s^{-1}$).

Figure 14 shows the evolution of the relative changes of total energy (bottom) and mass (top) for the runs with no diffusion and with e-folding time of 2 h for grid level 6. Figure 15 shows the evolution of the relative changes of total potential enstrophy (bottom) and the global mean vorticity (top). Although the model is not formally preserving potential enstrophy and total energy, these quantities are nearly conserved. It can be observed that the conservation properties of the model are not significantly affected by the amount of diffusion applied. Figure 16 shows the evolution of the kinetic energy relative to the initial total energy (bottom) and the evolution of the potential energy relative to the initial total energy (top) for the same runs. A transfer from potential to kinetic energy is observed.

3.3.2 Sensitivity to the wind reconstruction

The different reconstructions for the wind field as in test case 5 have been tried with the aim of testing the influence of the reconstruction on the model results. In all the cases the Asselin filter parameter is set to 0.1 and the e-folding time to 2 h.

Figure 17 shows the height (bottom) and wind (top) l_2 (solid lines) and l_∞ (dash-dotted lines) normalized errors for different grid levels for the different experiments.

For the height and vorticity field (not shown here), starting from grid level 3, the l_2 errors increase if more points are used for the reconstruction. The difference decrease with increasing grid level, and at grid level 6 all the experiments have similar l_2 height and vorticity errors. The l_∞ height and vorticity errors for the experiments with only 3 points stencil are smaller than the errors for the experiments with 9 and 15 points stencil at grid level 6. In the case of the wind field, the l_2 errors at grid level 6 for the experiments with a 3 points stencil are the largests. The wind is a diagnostic variable, to calculate the normalized wind errors, the wind has to be reconstructed from the normal velocity components and a bigger stencil yields smaller errors.

GMDD
2, 581–638, 2009

Again we can conclude that the used of a 15 points stencil is not recommended because it is more expensive and does not improve the model results. It is interesting to see that the experiments with a 3 points stencil have better results than the ones with a 9 points stencil, with the exception of the wind l_2 error at grid level 6.

3.3.3 Sensitivity to the Asselin filter

Experiments with different Asselin filter parameters (0.2, 0.1 and 0.08) have been run, with semi-implicit three-time-level scheme, RBF reconstruction with Gaussian kernel, 9 points stencil, scale factor 0.5 and e-folding time of 2 h.

The convergence plots for l_2 (solid lines) and l_∞ (dash-dotted lines) after 10 days for the height field are in Fig. 18.

The height l_2 and the wind (not shown here) l_2 normalized errors for the higher resolutions are reduced with decreasing Asselin filter parameter, the effect being larger in the case of the height field. On the contrary, in the case of the vorticity field, the errors decrease with increasing Asselin filter parameter, but the difference is very small and it is hardly seen in a convergence comparison plot.

The model solutions get numerically unstable for Asselin parameters of 0.05 and smaller for higher grid levels. Thus an Asselin filter parameter larger than 0.05 is needed for stability reasons.

4 Comparison to GMESWM

To evaluate the results of the ICOSWM model, a comparison with GMESWM, the shallow water version of GME (operational global model of Deutscher Wetterdienst, Majewski et al., 2002) has been considered.

The GMESWM model uses a non-staggered icosahedral-hexagonal grid. The prognostic variables are the height and zonal and meridional velocity components at the

centers of the hexagons/pentagons. The number of mass points is equal to the number of vorticity points for a given resolution.

The ICOSWM model uses a C-staggered grid, the prognostic variables are the height at the centers of the primary cells (the centers of the triangles) and the normal velocity components with respect to the cell edge. The vorticity is calculated at the centers of the dual grid (hexagons and pentagons) and the number of mass points is different from the number of vorticity points for a given grid level.

Convergence plots comparing the l_2 height and vorticity errors of ICOSWM and GMESWM for test cases 5 and 6 are shown in Figs. 19 and 20.

In GMESWM the number of equal intervals into which each side of the original icosahedral triangles is divided, n_i, is a natural parameter for specifying the resolution of the grid. GMESWM runs for n_i=32, 64, 96 and 192 corresponding to a spacing between grid points of about 240, 120, 80 and 40 km, with diffusion coefficients 8×10^{15}, 1×10^{15}, 4.22×10^{14} and 5×10^{13} $m^4\,s^{-1}$, respectively, have been considered. The Asselin parameter used in the GMESWM runs is 0.03.

The ICOSWM results in Figs. 19 and 20 correspond to a run with e-folding time of 2 h, RBF reconstruction with Gaussian kernel, 9 points stencil and scale factor 0.5, and Asselin filter 0.1.

For test case 5 (Fig. 19), ICOSWM shows a better height l_2 convergence rate and a similar vorticity l_2 convergence rate as GMESWM.

For test case 6 (Fig. 20), ICOSWM shows a better height l_2 convergence rate but a worse vorticity l_2 convergence rate than GMESWM. The vorticity is a diagnostic variable in both models and the different accuracy of the vorticity operators in both models could be one reason for this.

We can conclude that in general the ICOSWM results are better than those of GMESWM, probably due to the C-grid formulation and the Heikes-Randall grid optimization.

GMDD
2, 581–638, 2009

5 Kinetic energy spectra

In this section the kinetic energy spectra for some experiments are shown. They are also compared to the kinetic energy spectra of the variant of the NCAR STSWM used as a reference to evaluate the ICOSWM output fields.

The kinetic energy spectra are calculated using Eq. (11) (Eq. (3.2) in Jakob-Chien et al., 1995) where ζ_n^m and δ_n^m are the spectral coefficients of the divergence and the vorticity, n is the total wavenumber, m is the longitudinal wavenumber and a is the radius of the earth.

$$\overline{KE}_n = \frac{a^2}{4n(n+1)} \left[\zeta_n^0 (\zeta_n^0)^* + \delta_n^0 (\delta_n^0)^* + 2 \sum_{m=1}^{n} \zeta_n^m (\zeta_n^m)^* + 2 \sum_{m=1}^{n} \delta_n^m (\delta_n^m)^* \right] \tag{11}$$

To calculate the spectra, the divergence and vorticity fields are first interpolated to a Gaussian grid (T426 or T511). Then the spectral divergence and vorticity coefficients are calculated.

5.1 Test case 5 kinetic energy spectra

Figure 21 shows the kinetic energy spectra at day 15 for the NCAR STSWM model and ICOSWM with different e-folding times (three-time-level semi-implicit scheme, Asselin parameter 0.1, RBF reconstruction with Gaussian kernel, 9 points stencil and scale factor 0.5) for grid level 6.

There is a good agreement between the kinetic energy spectra of both models. Decreasing the e-folding time (increasing diffusion coefficients) in ICOSWM, the kinetic energy of the highest wavenumbers decreases.

5.2 Test case 6 kinetic energy spectra

Figure 22 shows the kinetic energy spectra at day 10 for the NCAR STSWM model and for ICOSWM with different e-folding times (three-time-level semi-implicit scheme,

GMDD
2, 581–638, 2009

Asselin parameter 0.1, RBF reconstruction with Gaussian kernel, 9 points stencil and scale factor 0.5) for grid level 6.

The energy corresponding to odd total wavenumbers is larger than the corresponding to even wavenumbers. The main contribution to the kinetic energy of the odd total wavenumbers is due to the vorticity spectral coefficients, since the zonal wavenumber m=4 dominates and the spherical harmonics for n odd and m=4 are antisymmetric with respect to the equator as is the vorticity field. The main contribution to the kinetic energy of the even total wavenumbers is due to the divergence spectral coefficients, because the zonal wavenumber m=4 dominates and the spherical harmonics for n even and m=4 are symmetric with respect to the equator as is the divergence field. This added to the fact that the vorticity field magnitude is larger than the divergence field magnitude, leads to the splitting observed in the spectra.

Divergence at initial time in test case 6 is zero, also the initial tendency of the divergence field. This initial state is a solution of the barotropic equations and in a barotropic model the solution would keep divergence free. In a shallow water model, some divergence is produced. The energy of the even wavenumbers for n>20 in the NCAR STSWM model is much smaller than in the ICOSWM, indicating that less divergence is produced by the NCAR STSWM model. Apart from this, there is a good agreement between the kinetic energy spectra of both models.

The kinetic energy spectra show a n^{-3} dependence for the odd wave numbers till wavenumbers of about 150. This is the same dependence that is observed in the large-scale part of the atmospheric kinetic energy spectra in the free troposphere and lower stratosphere (see e.g. Skamarock, 2004).

Decreasing the e-folding time (increasing diffusion coefficients) in ICOSWM, the kinetic energy of the even total wavenumbers for n>20 decreases, but for an e-folding time of 2 h, it is still much larger than in the NCAR STSWM kinetic energy spectrum. Decreasing the e-folding time also reduces the energy of the higher (odd and even) total wavenumbers. The odd wavenumber where the ICOSWM spectrum begins to decay due to the numerical explicit diffusion, can be used to define the effective resolution

GMDD
2, 581–638, 2009

of ICOSWM. This wavenumber is approximately 160, that corresponds to a wavelength of ∼250 km, that is ∼7 times the mean grid spacing. The NCAR STSWM kinetic energy spectrum can not be used as reference to define the effective resolution of ICOSWM as it is proposed in Skamarock (2004) because its tail is modified by the numerical diffusion used in the NCAR STSWM and can not be considered as the true spectrum.

To estimate the impact of the interpolation from the ICOSWM grid to the Gaussian grid on the calculated ICOSWM kinetic energy spectra , the spectrum of the initial state of test case 6 is considered. Figure 23 shows the spectra for the STSWM and ICOSWM models at initial time. The divergence is zero and the vorticity is a linear combination of the spherical harmonics $Y_{n=1}^{m=0}$ and $Y_{n=5}^{m=4}$ (Williamson et al., 1992). The spectra of both models show peaks at the expected total wavenumbers n=1 and n=5. The energy for the other total wavenumbers should be zero. Values for STSWM are typically $\sim 10^{-29}$, representing numerical noise, and $\sim 10^{-8}$ for ICOSWM. We can conclude that the accuracy of the ICOSWM spectra is limited to $\sim 10^{-8}$ due to the interpolation from the icosahedral grid to the Gaussian grid.

6 Conclusions

The results of the Icosahedral Shallow Water Model (ICOSWM) for tests cases 2, 5 and 6 of Williamson et al. (1992) are presented for a variety of model parameters. For test cases 5 and 6 the NCAR STSWM is used as reference. ICOSWM simulations for test cases 5 and 6 are better than GMESWM simulations, probably because of the C-grid formulation and the Heikes-Randall grid optimization. There is a good agreement between the kinetic energy spectra of ICOSWM and the spectra of the NCAR STSWM model.

In the framework of the ICON project a hydrostatic dynamical core has been developed (Wan, 2009) and a local grid refinement option and a non-hydrostatic dynamical core is under development. In these models new options for the divergence operator and the reconstruction of the wind have been implemented. The results presented here

are a reference to evaluate the impact that these new implementations and other new possible implementations coming have on the stability and quantitative results of the ICOSWM model.

References

Arakawa, A. and Lamb, V.: A potential enstrophy and energy conserving scheme for the shallow water equations, Mon. Weather Rev., 109, 18–136, 1981. 585, 588

Asselin, R.: Frequency filter for time integrations, Mon. Weather Rev., 100, 487–490, 1972. 588

Baumgardner, J. and Frederickson, P.: Icosahedral discretization of the two-sphere, SIAM Journal of Scientific Computing, 22, 1107–1115, 1985. 584

Bonaventura, L.: Development of the ICON dynamical core: modelling strategies and preliminary results, in: Proceedings of the ECMWF/SPARC Workshop on Modelling and Assimilation for the Stratosphere and Tropopause, 197–213, ECMWF, 2003. 583, 584, 585, 586, 587, 588

Bonaventura, L.: The ICON project: Development of a unified model using triangular geodesic grid, in: Proceedings of the ECMWF Annual Seminar on Development in Numerical Methods for Atmosphere and Ocean Modeling, 75–86, ECMWF, 2004. 583, 584, 585, 586, 587, 588

Bonaventura, L. and Ringler, T.: Analysis of discrete shallow water models on geodesic Delaunay grids with C-type staggering, Mon. Weather Rev., 133, 2351–2373, 2005. 584, 586, 588

Bonaventura, L., Kornblueh, L., Heinze, T., and Rípodas, P.: A semi-implicit method conserving mass and potential vorticity for the shallow water equations on the sphere, Int. J. Numer. Meth. Fl., 47, 863–869, 2005. 583, 584, 585, 586, 587, 588

Cullen, M.: Integration of the primitive barotropic equations on a sphere using the finite element method, Q. J. Roy. Meteorol. Soc., 100, 555–562, 1974. 584

Gassmann, A. and Heinze, T.: Icosahedral grid optimization strategies for triangular C grids, in: Proceedings of Solution of Partial Differential Equations on the sphere, 24–27 September 2007, Exeter, 2007. 586

Gill, A.: Atmosphere-Ocean Dynamics, Academic Press, 1982. 595

Giraldo, F. X.: Lagrange-Galerkin methods on spherical geodesic grids: The shallow water equations, J. Comp. Phys., 160, 336–368, 2000. 584

Heikes, R. and Randall, D.: Numerical integration of the shallow-water equations on a twisted icosahedral grid. Part I: Basic design and results of tests, Mon. Weather Rev., 123, 1862–1880, 1995a. 584

Heikes, R. and Randall, D.: Numerical integration of the shallow-water equations on a twisted icosahedral grid. Part II: A detailed description of the grid and an analysis of numerical accuracy, Mon. Weather Rev., 123, 1881–1887, 1995b. 586

Heinze, T. and Hense, A.: The Shallow Water Equations on the Sphere and their Lagrange-Galerkin solution, Meteorol. Atmos. Phys., 81, 129–137, 2002. 584

Hoskins, B.: Stability of the Rossby – Haurwitz wave, Q. J. Roy. Meteorol. Soc., 99, 723–745, 1973. 598

Jakob-Chien, R., Hack, J., and Williamson, D.: Spectral transform solutions to the shallow water test set, J. Comput. Phys., 119, 164–187, 1995. 583, 603

Lin, S. and Rood, R.: An explicit flux-form semi-Lagrangian shallow water model on the sphere, Q. J. Roy. Meteorol. Soc., 123, 2477–2498, 1997. 585, 588

Majewski, D., Liermann, D., Prohl, P., Ritter, B., Buchhold, M., Hanisch, T., Paul, G., Wergen, W., and Baumgardner, J.: The operational global icosahedral-hexagonal gridpoint model GME: description and high resolution tests, Mon. Weather Rev., 130, 319–338, 2002. 585, 601

Narcowich, F. and Ward, J.: Generalized Hermite interpolation via matrix-valued conditionally positive definite functions, Math. Comput., 63, 661–687, 1994. 587

Quarteroni, A. and Valli, A.: Numerical approximation of partial differential equations, chap. 9: The Stokes problem, Springer Verlag, 1994. 587

Quiang, D., Gunzburger, M., and Lili, J.: Voronoi-based finite volume methods, optimal Voronoi meshes and PDEs on the sphere, Comput. Method. Appl. M., 192, 3933–3957, 2003. 584

Raviart, P. and Thomas, J.: A mixed finite element method for 2nd order elliptic problems., in: Mathematical aspects of finite element methods, 292–315, Springer Verlag, 1977. 587

Ringler, T. and Randall, D.: A potential enstrophy and energy conserving numerical scheme for solution of the shallow-water equations a geodesic grid, Mon. Weather Rev., 130, 1397–1410, 2002. 584, 585, 588

Ringler, T., Heikes, R., and Randall, D.: Modeling the atmospheric general circulation using a spherical geodesic grid: A new class of dynamical cores, Mon. Weather Rev., 128, 2471–2490, 2000. 584

Ruppert, T.: Diploma-thesis. Vector Field Reconstruction by Radial Basis Functions, Tech. Rep.

1089046, TU Darmstadt, 2007. 587, 593
Sadourny, R.: The dynamics of finite difference models of the shallow water equations, J. Atmos. Sci., 32, 680–689, 1975. 585, 588
Skamarock, W. C.: Evaluating Mesoscale NWP Models Using Kinetic Energy Spectra, Mon. Weather Rev., 132, 3019–3032, 2004. 604, 605
Smith, R. and Dritschel, D.: Revisiting the Rossby-Haurwitz wave test case with contour advection, J. Comp. Phys., 217, 473–484, 2006. 598
Thuburn, J. and Li, Y.: Numerical simulation of Rossby-Haurwitz waves, Tellus A, 52, 181–189, 2000. 598
Wan, H.: Developing and testing a hydrostatic atmospheric dynamical core on triangular grids, Reports on Earth System Science No. 65, Max Planck Institute for Meteorology, Hamburg, Germany, online available at: http://www.mpimet.mpg.de/en/wissenschaft/publikationen/erdsystemforschung.html#c2612, 2009. 605
Williamson, D., Drake, J., Hack, J., Jakob, R., and Swarztrauber, R.: A standard test set for numerical approximations to the shallow water equations in spherical geometry, J. Comp. Phys., 102, 221–224, 1992. 583, 590, 595, 598, 605

Table 1. The triangular icosahedral grid at various resolutions: number of grid points.

Level	Mass points	Velocity points	Vorticity points
−1	20	30	12
0	80	120	42
1	320	480	162
2	1280	1920	642
3	5120	7680	2562
4	20 480	30 720	10 242
5	81 920	122 880	40 962
6	327 680	491 520	163 842

GMDD
2, 581–638, 2009

Table 2. The triangular icosahedral grid at various resolutions: minimum, mean and maximum distances between grid points and velocity point off-centering (Eq. 1). Radius of the Earth: 6.371229×10^6 m.

Level	min/mean/max distances (km) between mass points	min/mean/max distances (km) between vorticity points	off-centering, %
0	2004.8/2251.1/2497.4	3526.9/3765.0/4003.2	9.97
1	784.3/1116.2/1385.4	1701.8/1916.2/2117.3	5.97
2	345.3/556.9/714.7	843.1/962.3/1079.9	3.34
3	163.3/278.3/360.9	421.4/481.6/541.7	1.78
4	80.1/139.1/181.5	210.3/240.9/271.3	0.97
5	39.9/69.5/91.0	105.0/120.5/135.8	0.61
6	19.8/34.8/45.7	52.4/60.2/67.9	0.40

GMDD
2, 581–638, 2009

Table 3. Approximate minimum, mean and maximum diffusion coefficients ($m^4\ s^{-1}$) corresponding to an e-folding time of 28 h for different grid levels.

Level	min k_4 ($m^4\ s^{-1}$)	mean k_4 ($m^4\ s^{-1}$)	max k_4 ($m^4\ s^{-1}$)
2	2.20367e+15	1.4899e+16	4.0444e+16
3	1.10231e+14	9.28513e+14	2.6297e+15
4	6.38101e+12	5.80321e+13	1.68216e+14
5	3.92872e+11	3.61659e+12	1.06298e+13
6	2.38243e+10	2.2734e+11	6.76121e+11

GMDD
2, 581–638, 2009

Table 4. Approximate minimum, mean and maximum diffusion coefficients ($m^4\,s^{-1}$) corresponding to an e-folding time of 2 h for different grid levels.

Level	min k_4 ($m^4\,s^{-1}$)	mean k_4 ($m^4\,s^{-1}$)	max k_4 ($m^4\,s^{-1}$)
2	3.08513e+16	2.08586e+17	5.66217e+17
3	1.54324e+15	1.29992e+16	3.68159e+16
4	8.93342e+13	8.12449e+14	2.35502e+15
5	5.50021e+12	5.06322e+13	1.48817e+14
6	3.3354e+11	3.18276e+12	9.46569e+12

Table 5. Normalized l_2 and l_∞ errors after 10 days run. Case 2 with zonal flow. e-Folding time 2 h, Asselin filter parameter 0.1, RBF reconstruction, Gaussian kernel, 9 points stencil, scale factor 0.5.

	height		wind		vorticity	
Level	l_2	l_∞	l_2	l_∞	l_2	l_∞
2	0.257e-2	0.544e-2	0.439e-1	0.785e-1	0.177	0.249
3	0.529e-3	0.112e-2	0.913e-2	0.160e-1	0.375e-1	0.556e-1
4	0.123e-3	0.270e-3	0.212e-2	0.364e-2	0.912e-2	0.194e-1
5	0.300e-4	0.661e-4	0.518e-3	0.897e-3	0.234e-2	0.655e-2
6	0.740e-5	0.163e-4	0.129e-3	0.220e-3	0.660e-3	0.206e-2

GMDD
2, 581–638, 2009

Table 6. Normalized l_2 and l_∞ errors after 15 days run. Case 5. e-Folding time 2 h, Asselin filter parameter 0.1, RBF reconstruction, Gaussian kernel, 9 points stencil, scale factor 0.5.

	height		wind		vorticity	
Level	l_2	l_∞	l_2	l_∞	l_2	l_∞
2	0.983e-2	0.382e-1	0.353	0.436	0.663	0.628
3	0.248e-2	0.916e-2	0.120	0.198	0.300	0.306
4	0.879e-3	0.331e-2	0.429e-1	0.699e-1	0.138	0.196
5	0.514e-3	0.271e-2	0.153e-1	0.413e-1	0.596e-1	0.165
6	0.338e-3	0.200e-2	0.648e-2	0.231e-1	0.260e-1	0.120

GMDD
2, 581–638, 2009

Table 7. Normalized l_2 and l_∞ errors after 10 days run. Case 6. e-Folding time 2 h, Asselin filter parameter 0.1, RBF reconstruction, Gaussian kernel, 9 points stencil, scale factor 0.5.

	height		wind		vorticity	
Level	l_2	l_∞	l_2	l_∞	l_2	l_∞
2	0.473e-1	0.114	0.733	0.898	1.083	1.048
3	0.154e-1	0.367e-1	0.222	0.265	0.357	0.412
4	0.408e-2	0.111e-1	0.582e-1	0.753e-1	0.126	0.199
5	0.130e-2	0.433e-2	0.175e-1	0.278e-1	0.773e-1	0.167
6	0.474e-3	0.191e-2	0.566e-2	0.180e-1	0.598e-1	0.141

GMDD
2, 581–638, 2009

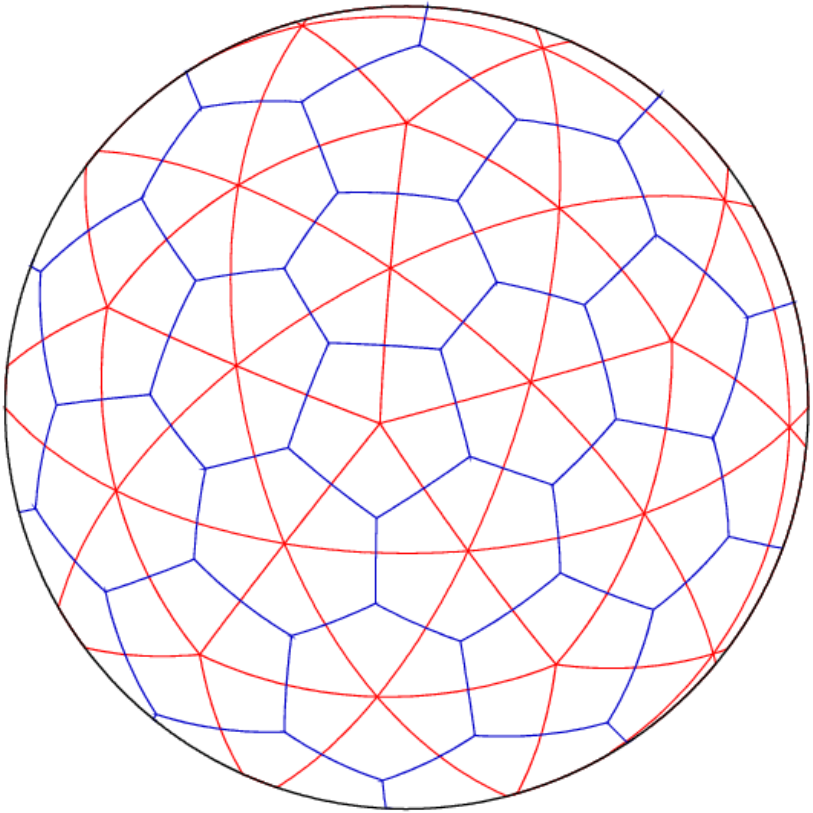

Fig. 1. Delaunay (red triangles) and Voronoi (blue hexagons, and pentagons at the 12 special points) grids on the sphere obtained after one dyadic refinement step of the regular icosahedron.

GMDD

2, 581–638, 2009

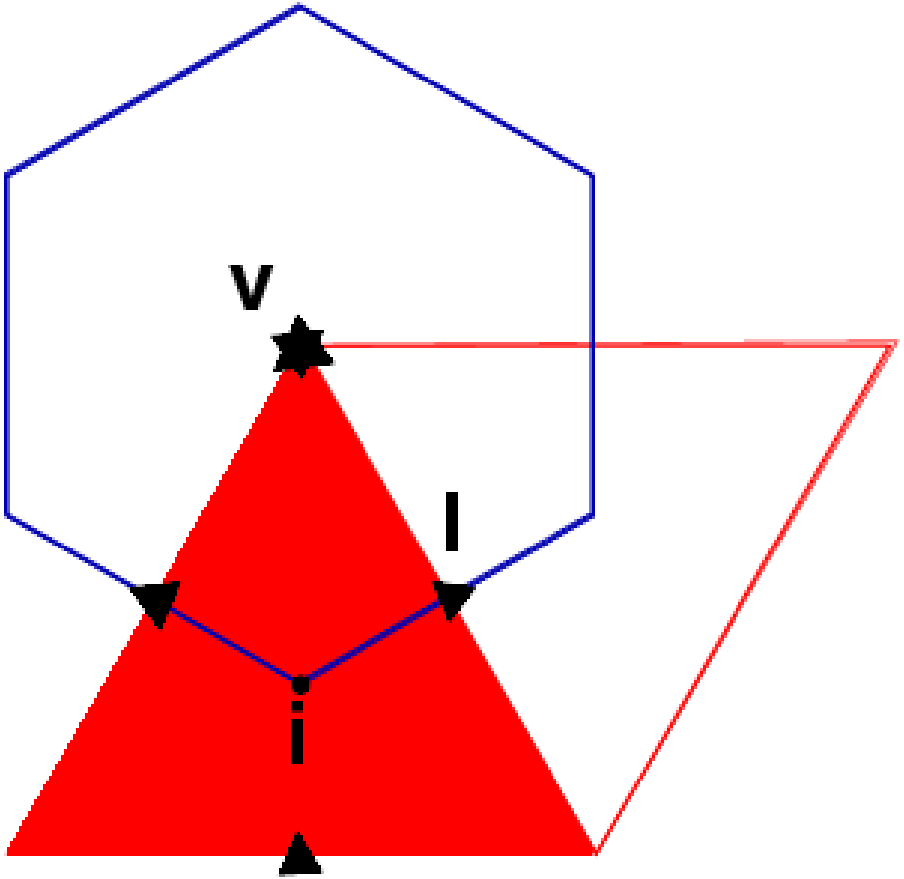

Fig. 2. C-grid type staggering of variables in ICOSWM. Mass point "*i*", normal velocity point "*l*" and vorticity point "*v*".

GMDD
2, 581–638, 2009

Icosahedral Shallow Water Model (ICOSWM)

P. Rípodas et al.

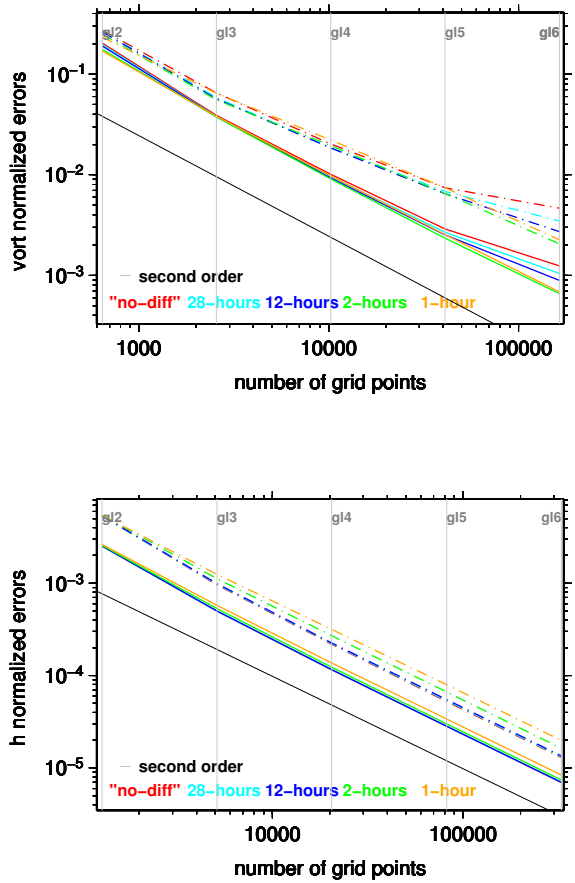

Fig. 3. Height field (bottom) and vorticity field (top) convergence test for case 2 with zonal flow after 10 days. Tests for different e-folding times. Solid lines for l_2 errors and dash-dotted lines for l_∞ errors.

GMDD
2, 581–638, 2009

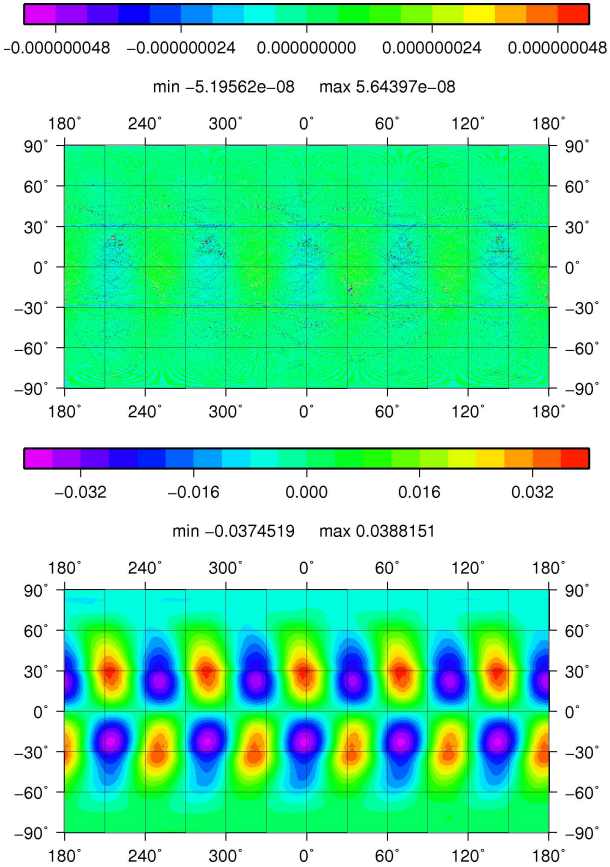

Fig. 4. Errors of the height field (bottom) and vorticity field (top) after 10 days for test case 2 without explicit diffusion.

GMDD
2, 581–638, 2009

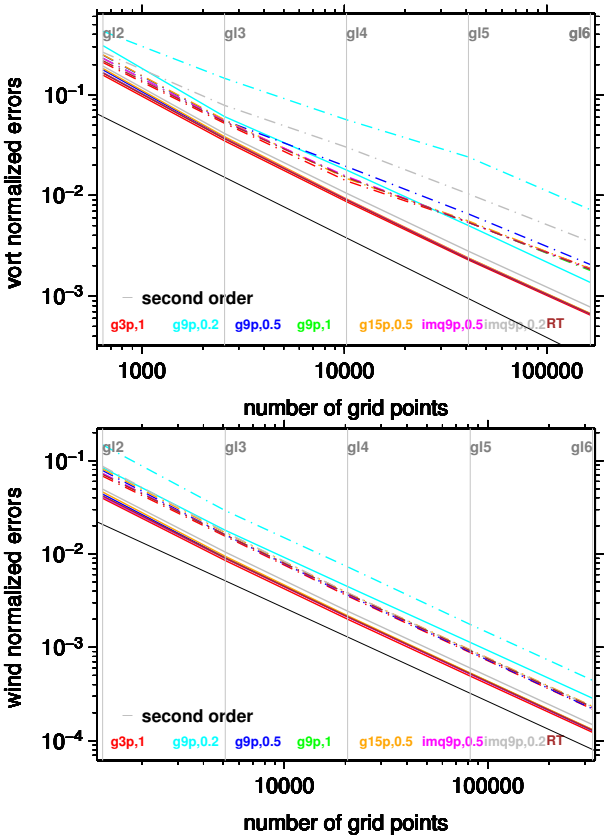

Fig. 5. Wind field (bottom) and vorticity field (top) convergence test for case 2 with zonal flow after 10 days. Tests for different wind reconstructions. Solid lines for l_2 errors and dash-dotted lines for l_∞ errors.

GMDD
2, 581–638, 2009

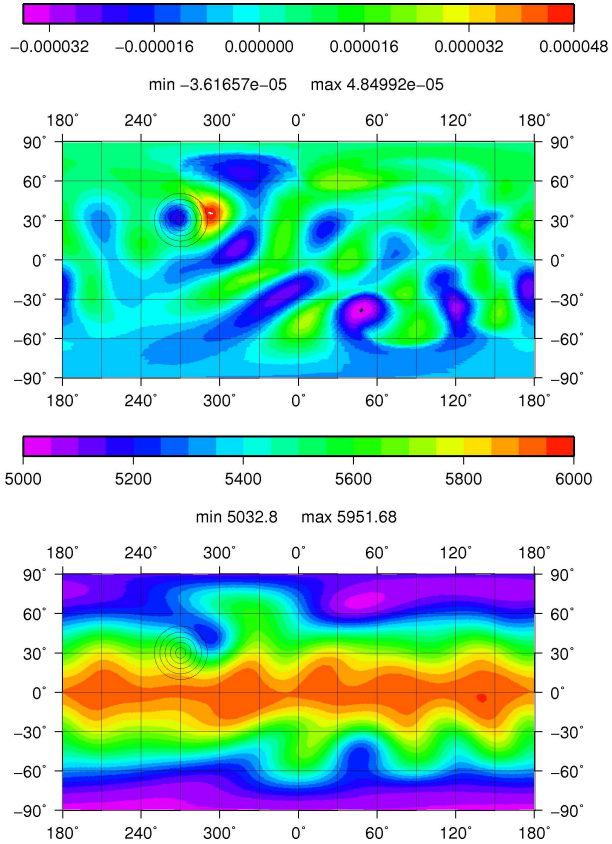

Fig. 6. ICOSWM height (m) (bottom) and vorticity (s^{-1}) (top) fields after 15 days. Test case 5. Grid level 6.

GMDD
2, 581–638, 2009

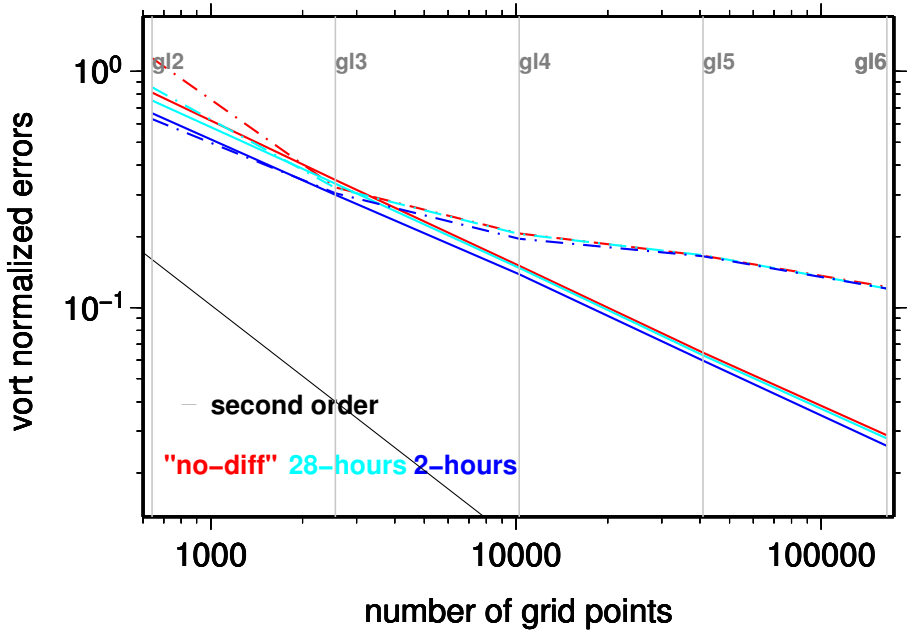

Fig. 7. Vorticity field convergence test for case 5 after 15 days. Tests for different e-folding times. Solid lines for l_2 errors and dash-dotted lines for l_∞ errors.

GMDD
2, 581–638, 2009

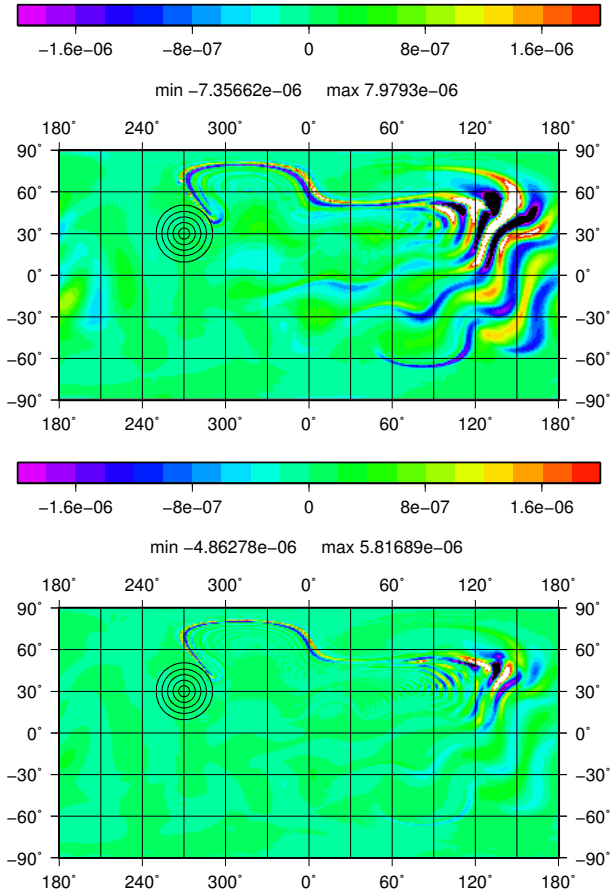

Fig. 8. Differences ICOSWM-NCAR STSWM for the vorticity field (s^{-1}) after 15 days for test case 5. Grid level 6 (bottom) and grid level 5 (top).

GMDD
2, 581–638, 2009

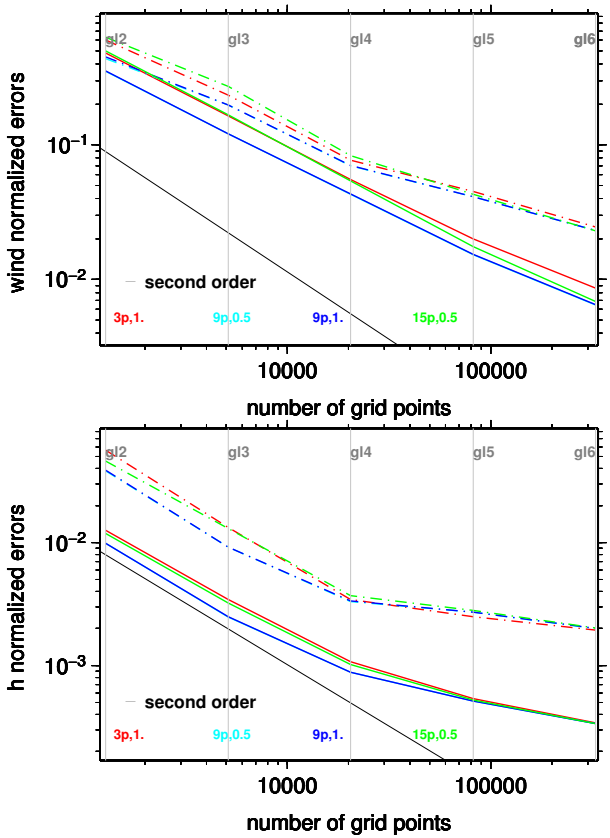

Fig. 9. Height field (bottom) and wind field (top) convergence test for case 5 after 15 days. Tests for different wind reconstructions. Solid lines for l_2 errors and dash-dotted lines for l_∞ errors.

GMDD
2, 581–638, 2009

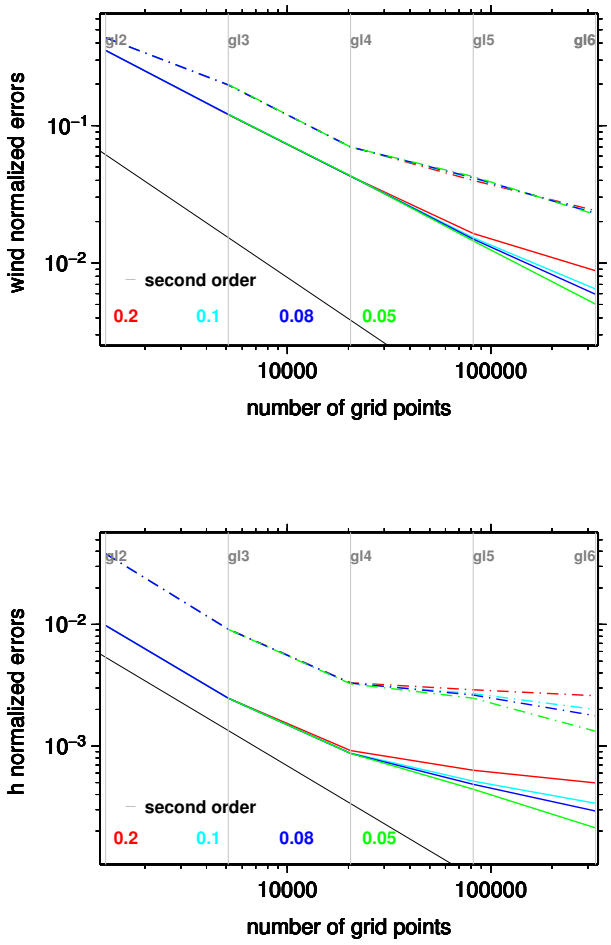

Fig. 10. Height field (bottom) and wind field (top) convergence test for case 5 after 15 days. Tests for different Asselin filter parameters. Solid lines for l_2 errors and dash-dotted lines for l_∞ errors.

GMDD
2, 581–638, 2009

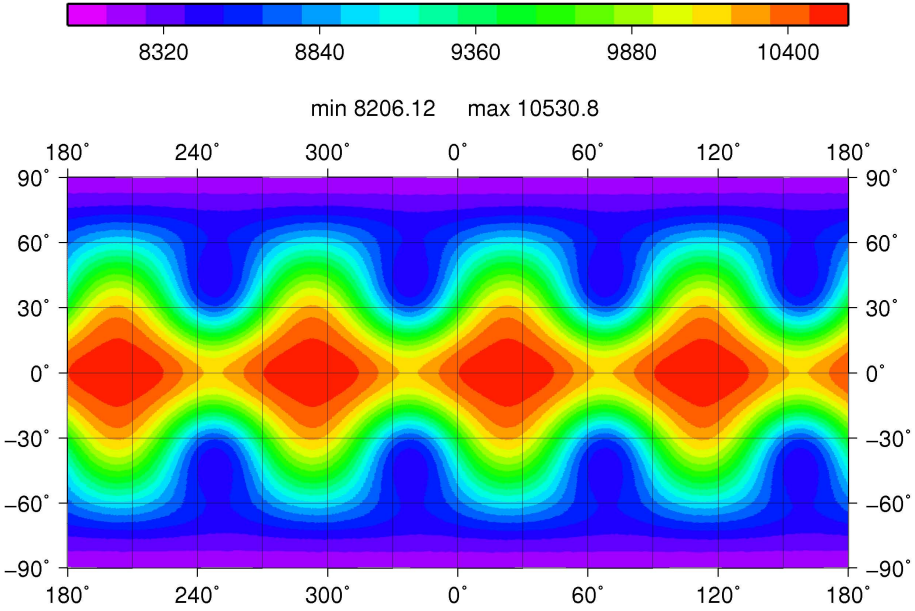

Fig. 11. ICOSWM height field (m) after 10 days. Test case 6. Grid level 6.

GMDD
2, 581–638, 2009

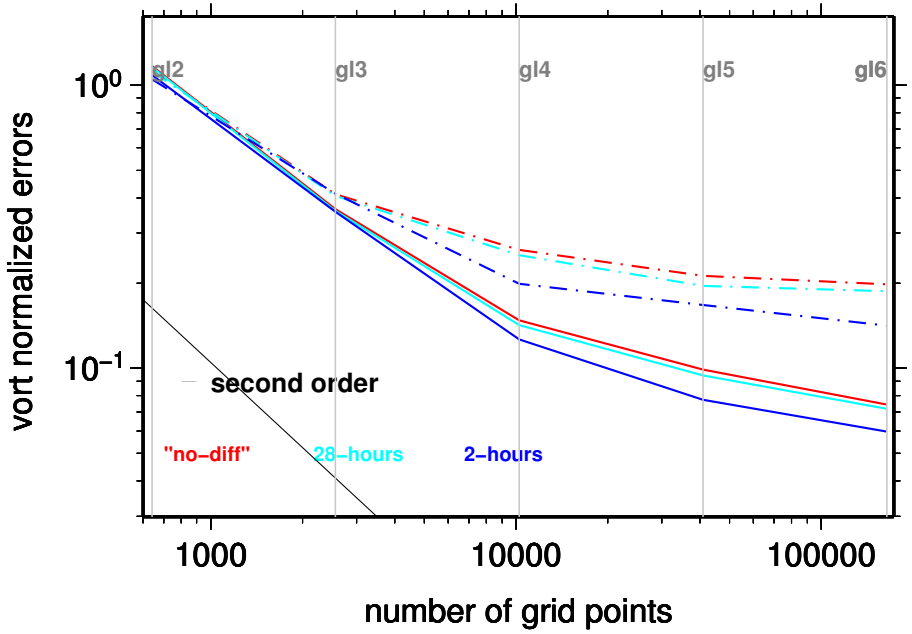

Fig. 12. Vorticity field convergence test for case 6 after 10 days. Tests for different e-folding times. Solid lines for l_2 errors and dash-dotted lines for l_∞ errors.

GMDD
2, 581–638, 2009

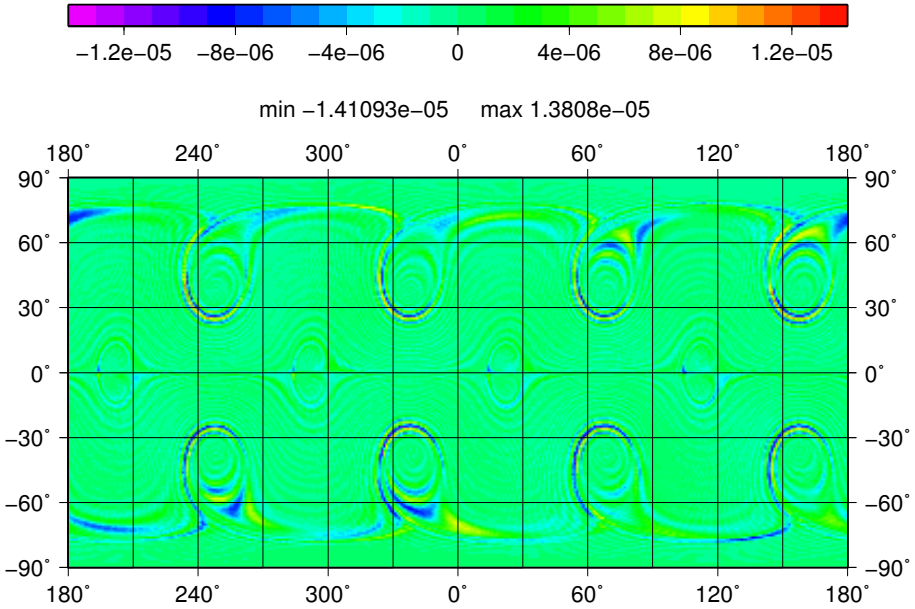

Fig. 13. Difference ICOSWM-NCAR STSWM for the vorticity field (s^{-1}) after 10 days for test case 6, grid level 6.

GMDD
2, 581–638, 2009

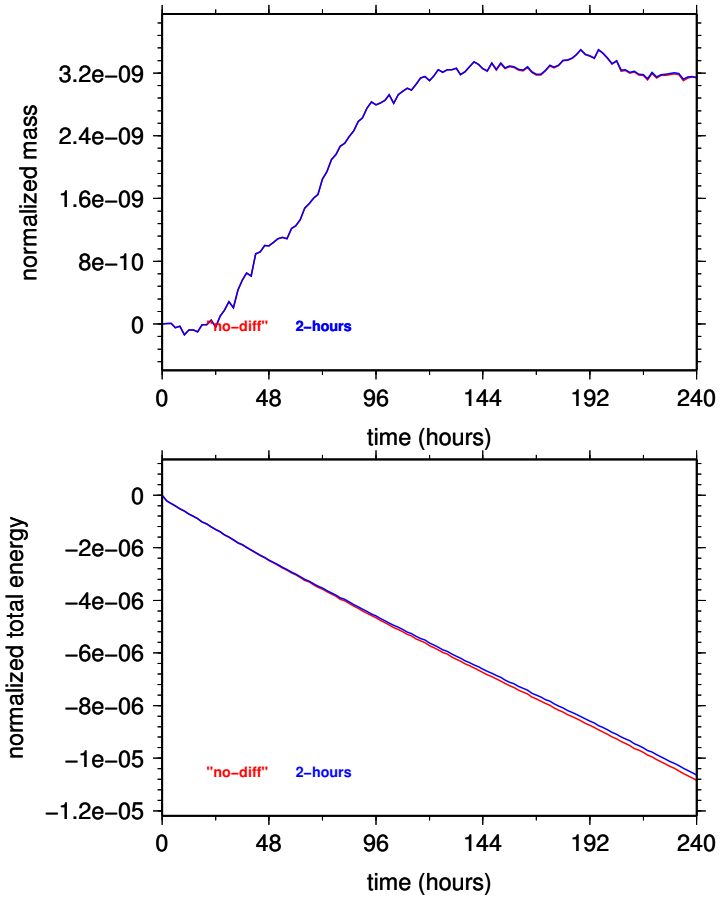

Fig. 14. Relative changes of total energy (bottom) and total mass (top). Case 6. Grid level 6.

GMDD
2, 581–638, 2009

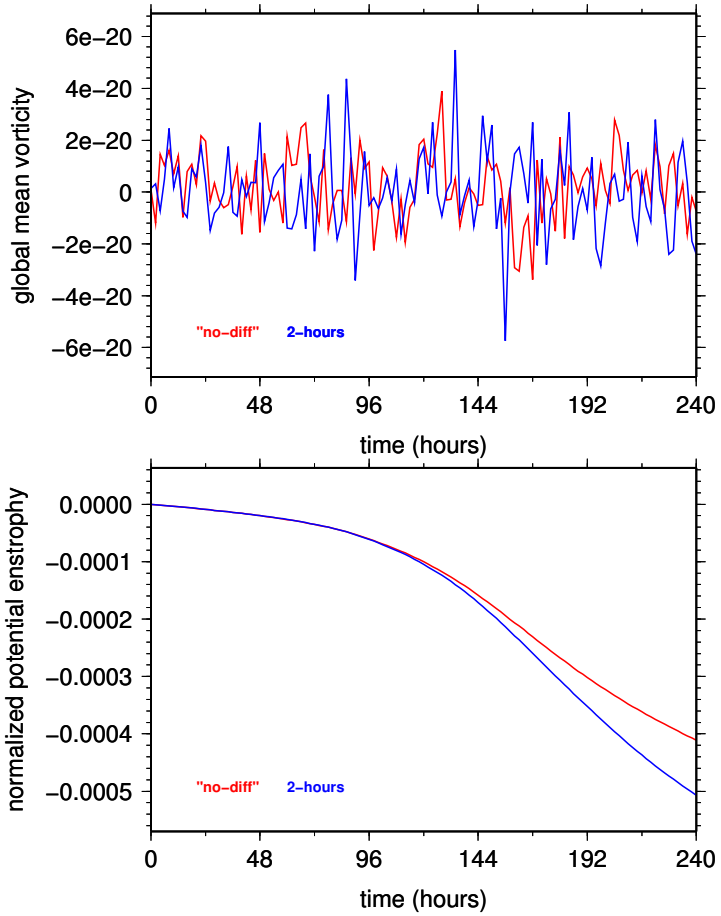

Fig. 15. Relative changes of the total potential enstrophy (bottom) and evolution of the global mean vorticity (top). Case 6. Grid level 6.

GMDD
2, 581–638, 2009

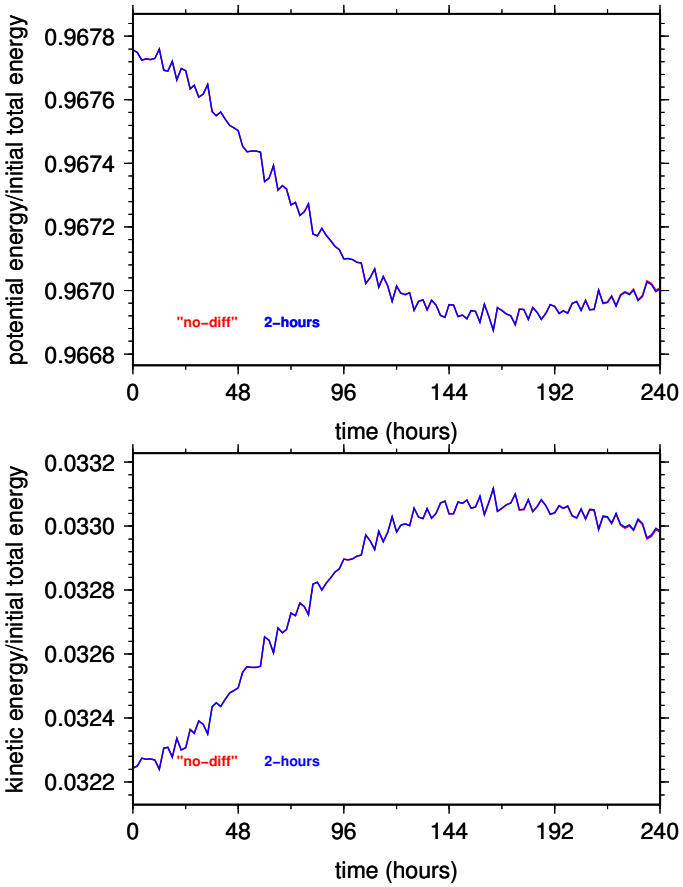

Fig. 16. Evolution of kinetic energy (bottom) and potential energy (top) relatives to the initial total energy. Case 6. Grid level 6.

GMDD
2, 581–638, 2009

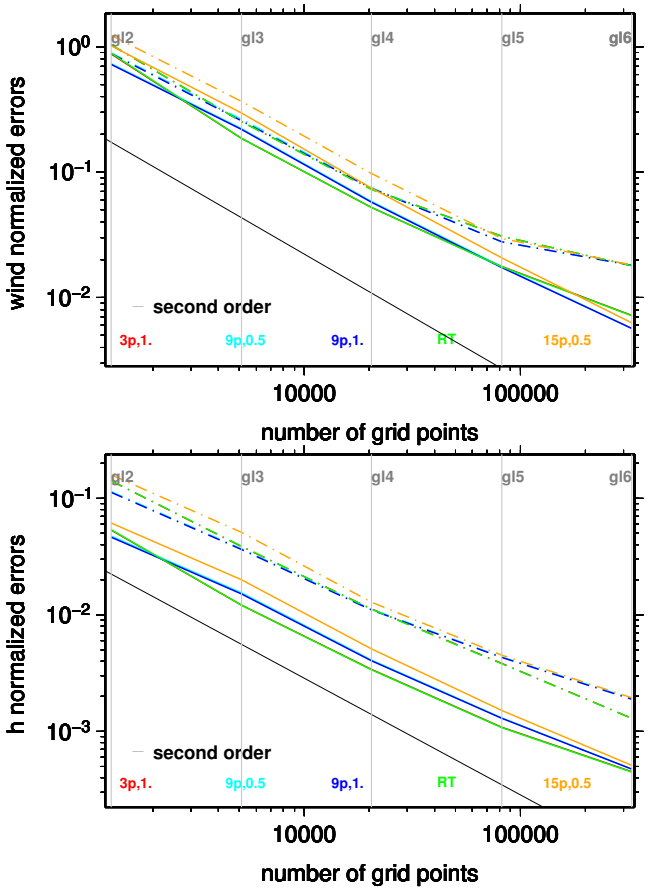

Fig. 17. Height field (bottom) and wind field (top) convergence test for case 6 after 10 days. Tests for different wind reconstructions. Solid lines for l_2 errors and dash-dotted lines for l_∞ errors.

GMDD
2, 581–638, 2009

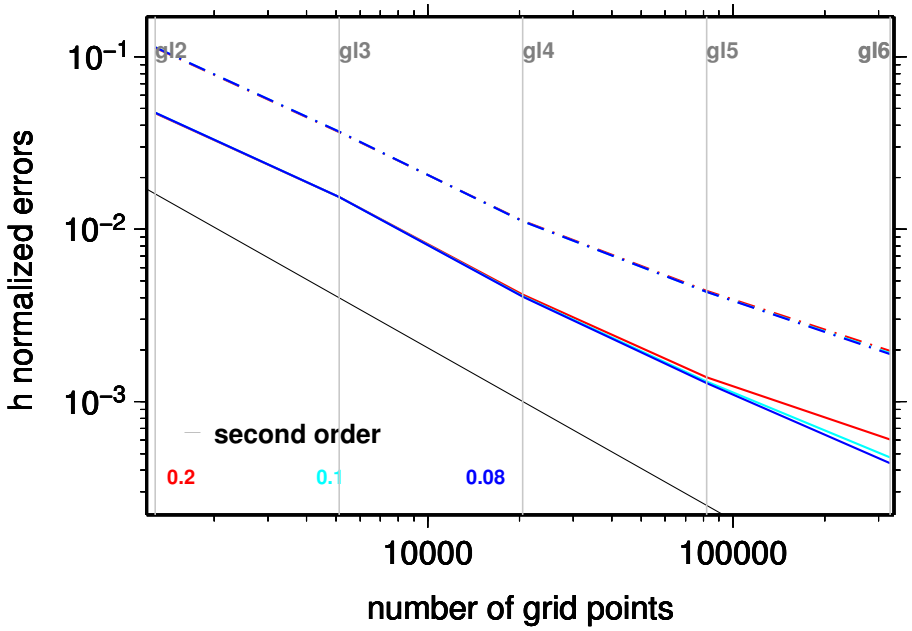

Fig. 18. Height field convergence test for case 6 after 10 days. Tests for different e-folding times. Solid lines for l_2 errors and dash-dotted lines for l_∞ errors.

GMDD
2, 581–638, 2009

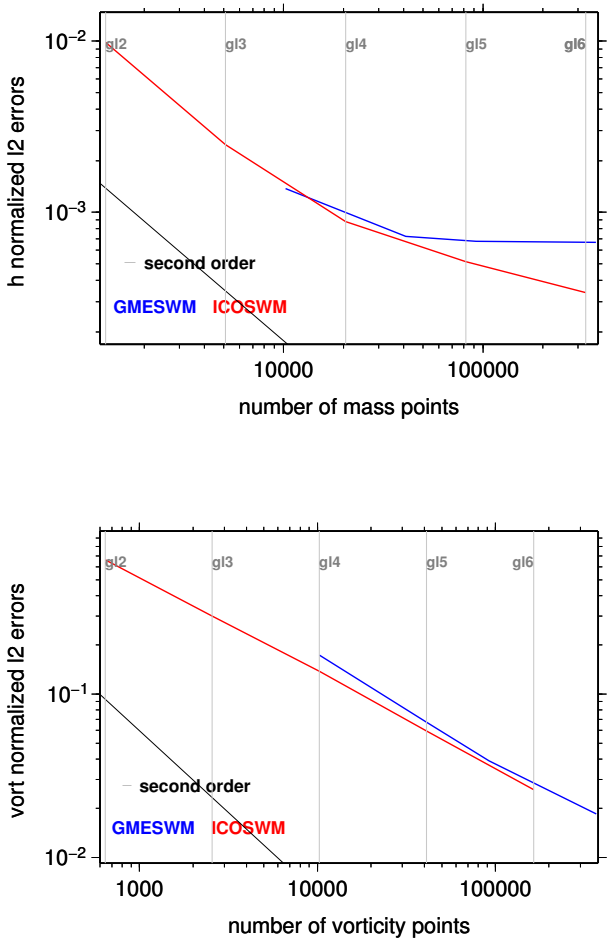

Fig. 19. Convergence test after 15 days. Test case 5. Comparison GMESWM and ICOSWM. Top: height field; bottom: vorticity field.

GMDD
2, 581–638, 2009

Title Page
Abstract Introduction
Conclusions References
Tables Figures
◀I ▶I
◀ ▶
Back Close
Full Screen / Esc
Printer-friendly Version
Interactive Discussion

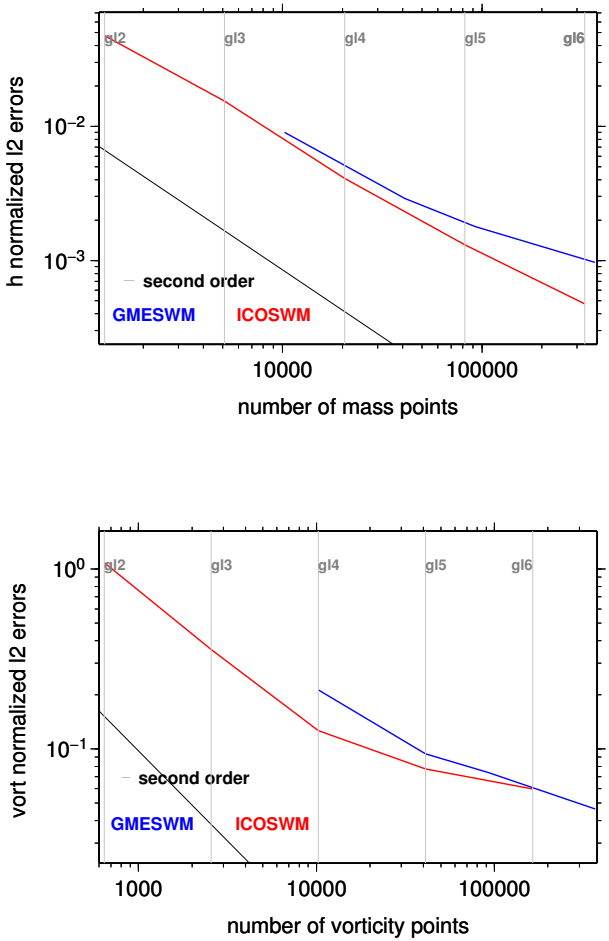

Fig. 20. Convergence test after 10 days. Test case 6. Comparison GMESWM and ICOSWM. Top: height field; bottom: vorticity field.

GMDD
2, 581–638, 2009

Title Page
Abstract Introduction
Conclusions References
Tables Figures
◀| |▶
◀ ▶
Back Close
Full Screen / Esc
Printer-friendly Version
Interactive Discussion

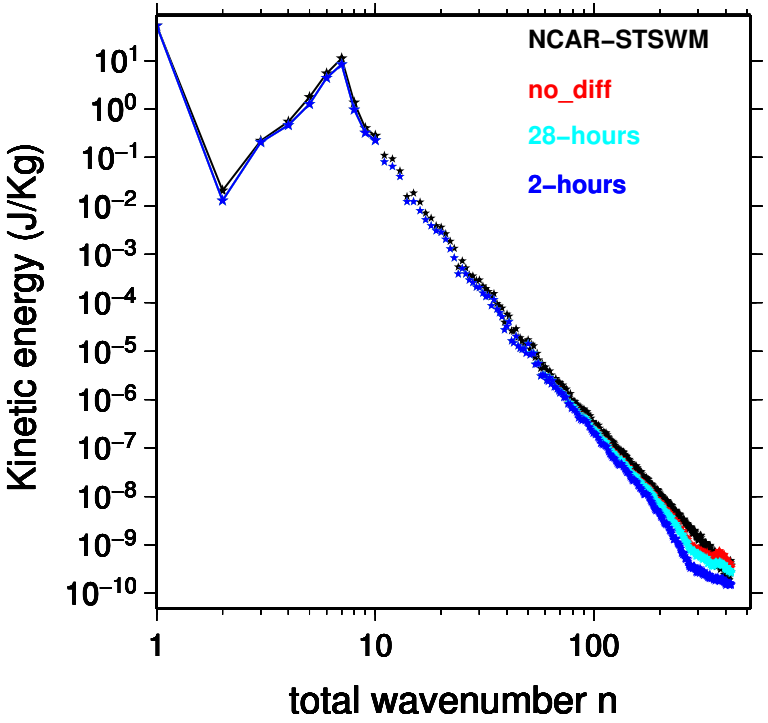

Fig. 21. Kinetic energy spectra after 15 days run, case 5. T426 NCAR STSWM model and ICOSWM model grid level 6 with different e-folding times.

GMDD
2, 581–638, 2009

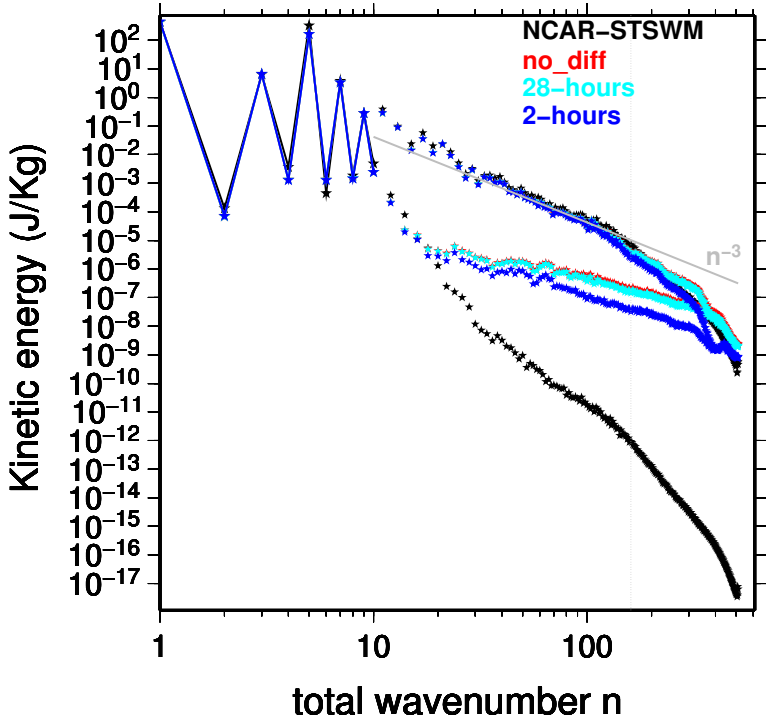

Fig. 22. Kinetic energy spectra after 10 days run, case 6. T511 NCAR STSWM model and ICOSWM model grid level 6 with different e-folding times.

GMDD
2, 581–638, 2009

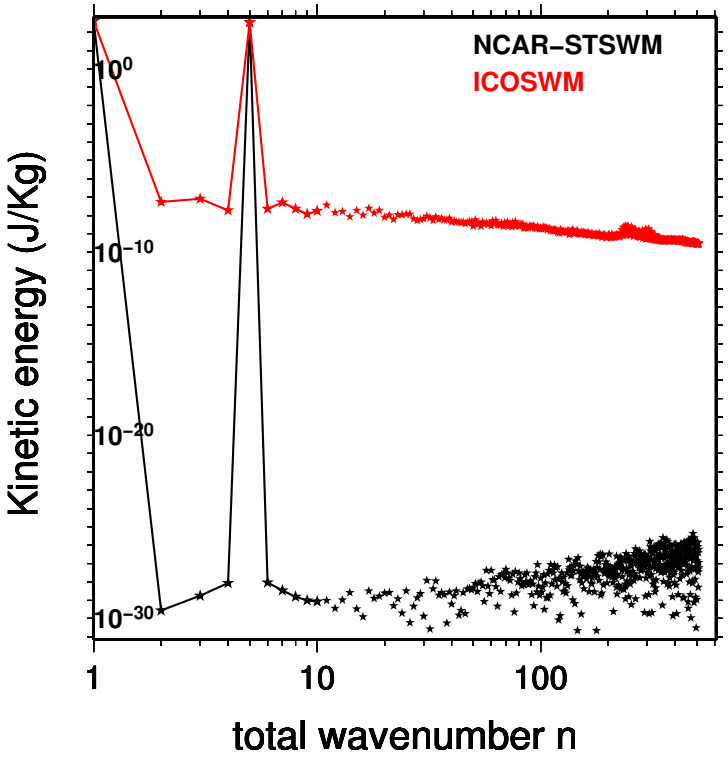

Fig. 23. Kinetic energy spectra at initial time, case 6. T511 NCAR STSWM model and ICOSWM model grid level 6.

GMDD
2, 581–638, 2009